

1   **Reconstruction of genetically identified neurons imaged by serial-section**  
2   **electron microscopy.**

3

4   Maximilian Joesch<sup>1</sup>, David Mankus<sup>1</sup>, Masahito Yamagata<sup>1</sup>, Ali Shahbazi<sup>2</sup>, Richard  
5   Schalek<sup>1</sup>, Adi Suissa-Peleg<sup>3</sup>, Markus Meister<sup>4</sup>, Jeff W. Lichtman<sup>1</sup>, Walter J. Scheirer<sup>2</sup>,  
6   Joshua R. Sanes<sup>1</sup>

7

8

9   1. Center for Brain Science and Department of Molecular and Cellular Biology, Harvard  
10   University, Cambridge, MA.

11

12   2. University of Notre Dame, Notre Dame, IN.

13   3. School of Engineering and Applied Sciences, Harvard University, Cambridge, MA.

14   4. Division of Biology, California Institute of Technology, Pasadena, CA.

15

16

17

18   Correspondence should be addressed to J.R.S. (sanes@mcb.harvard.edu)

19 **ABSTRACT**

20 **Resolving patterns of synaptic connectivity in neural circuits currently requires**  
21 **serial section electron microscopy. However, complete circuit reconstruction is**  
22 **prohibitively slow and may not be necessary for many purposes such as**  
23 **comparing neuronal structure and connectivity among multiple animals. Here, we**  
24 **present an alternative strategy, targeted reconstruction of specific neuronal types.**  
25 **We used viral vectors to deliver peroxidase derivatives, which catalyze**  
26 **production of an electron-dense tracer, to genetically identified neurons, and**  
27 **developed a protocol that enhances the electron-density of the labeled cells and**  
28 **while retaining quality of the ultrastructure. The high contrast of the marked**  
29 **neurons enabled two innovations that dramatically speed data acquisition:**  
30 **targeted high-resolution reimaging of regions selected from rapidly-acquired**  
31 **lower resolution reconstruction, and an unsupervised segmentation algorithm.**  
32 **This pipeline reduces imaging and reconstruction times by at least two orders of**  
33 **magnitude, facilitating directed inquiry of circuit motifs.**

34

35 **INTRODUCTION**

36 Relating neural circuits to the computations they perform requires mapping patterns of  
37 structural and functional connectivity among neurons. Innovative light microscopic  
38 methods such as GRASP, trans-synaptic viral tracing and super-resolution imaging  
39 enable visualization of synapses made on or by identified neurons<sup>1,2</sup>. At present,  
40 however, only electron microscopy (EM) provides sufficient resolution to visualize the  
41 complete complement of synapses that neurons form and receive. Indeed, large-scale

42 reconstructions from serial sections have provided deep insights into neuronal circuit  
43 principles<sup>3–6</sup>. The optimal strategy is to collect serial sections containing all circuit  
44 elements and image them at nanometer resolution. Processes in the imaged volumes  
45 are then segmented to reconstruct the neurons (or parts of neurons) they contain.  
46 Advances in sectioning, imaging and segmentation methods make so-called “saturated”  
47 reconstruction of volumes around 1000 μm<sup>3</sup> feasible<sup>7</sup>. Even these modest volumes  
48 remain challenging, however, and when multiple samples must be compared -e.g.,  
49 controls vs. mutant or treated vs. untreated animals - this approach is currently out of  
50 reach<sup>8</sup>.

51

52 An attractive alternative is “sparse” reconstruction of specific cells within a fully imaged  
53 volume. For example, neuronal activity can be monitored using calcium indicators, then  
54 neurons with particular patterns of activity can be relocated in thin sections and  
55 reconstructed<sup>3,4</sup>. This method is, however, technically demanding and infeasible in  
56 many tissues. We therefore devised an alternative approach to sparse reconstruction  
57 that relies on marking specific cells with an electron-dense tracer. We then exploit the  
58 high contrast provided by the tracer to speed up imaging and reconstruction, which are  
59 currently the rate-limiting steps in connectomic analysis. Our pipeline includes the  
60 following series of steps: (a) tagging a specific cell type with a genetically encoded EM  
61 tracer, (b) enhancing the electron-density of the stain without compromising  
62 ultrastructure of the surrounding tissue, (c) imaging the cell rapidly at relatively low  
63 resolution, (d) re-imaging selected small volumes at higher resolution to map  
64 connectivity and (e) segmenting the cell using a novel algorithm that is reliable, fast and

65 does not require computationally intense pre-training. Together, the gains from targeted  
66 reimaging and unsupervised segmentation decrease the time required for  
67 reconstruction by over two orders of magnitude. We call the method ARTEMIS for  
68 Assisted Reconstruction Technique for Electron Microscopic Interrogation of Structure.

69

70 **RESULTS AND DISCUSSION**

71 A classical ultrastructural tracer is horseradish peroxidase (HRP), which catalyzes the  
72 formation of a 3,3'-diaminobenzidine (DAB) polymer; the polymer binds osmium and is  
73 thereby rendered electron-dense. Recombinant HRP is enzymatically inactive in the  
74 cytosol because it fails to form disulfide bonds or become glycosylated, but this  
75 limitation can be overcome by directing the protein to topologically extracellular  
76 compartments such as vesicles<sup>9–11</sup>. We therefore generated an HRP variant that was  
77 codon-optimized, mutated to increase activity, and fused to an endoplasmic  
78 reticulum targeting sequence (erHRP). We also tested derivatives of plant ascorbate  
79 peroxidases called APX and APEX2, which are active in the cytosol<sup>12,13</sup>. Initial studies  
80 using cultured HEK293 cells confirmed that all three constructs generated active  
81 peroxidase in the transfected cells (Fig. 1a,b and data not shown).

82

83 For selective expression in molecularly-identified cells, we generated adeno-associated  
84 viral (AAV) vectors in which expression of erHRP, APX or APEX2 required Cre-  
85 dependent recombination. These were used to infect retinas of transgenic mice in which  
86 specific retinal ganglion cell (RGC) types expressed Cre recombinase (ooDSGCs in  
87 Cart-Cre<sup>14</sup>) or tamoxifen-activated Cre (J-RGCs in JAM-B-CreER<sup>15</sup>). Two to four weeks  
88 after infection, retinas were reacted with DAB and H<sub>2</sub>O<sub>2</sub> and examined light

89 microscopically, revealing intense labeling of RGCs (Fig. 1c,d). Retinas were then  
90 processed for EM (see Methods). Unexpectedly, levels of electron-dense precipitate  
91 were so low that stained processes could not be traced reliably (Figure 1 – Figure  
92 Supplement 1a,b). Numerous alterations to balance peroxidase activity and  
93 ultrastructural quality failed to improve matters: when ultrastructure was adequately  
94 preserved, staining for peroxidase was poor, and when reaction product was adequate,  
95 synaptic structures were poorly preserved. This difficulty may have been less apparent  
96 in previous studies using injected native HRP, which has substantially higher activity  
97 than the recombinant proteins we use.

98

99 The reason for the difference between light and electron microscopic results is likely  
100 that the opacity and electron density of the DAB polymer arise in different ways: its  
101 polycyclic structure renders it photon absorbent, but its electron-density results from  
102 redox reactions with osmium<sup>16</sup>. We reasoned that radicals produced during the long  
103 peroxidase reaction might oxidize the relevant functional groups in the polymer, leaving  
104 it photon-absorbent but inert to osmium. If this were true, reduction of functional groups  
105 on the polymer could restore reactivity to osmium (Fig. 1e). We tested this hypothesis in  
106 transfected HEK cells. When cells were treated with the protocol we had used for retina,  
107 precipitate was clearly visible by light but not electron microscopy. However, when the  
108 HEK cells were treated with a mild reducing agent (5 mM sodium hydrosulfite) between  
109 the peroxidase reaction and osmication, they were highly electron-dense (Fig. 1f, g).  
110 This was the case using either conventional osmium staining or an enhanced “double  
111 osmium” staining protocol (rOTO), although the latter shows a slight improvement

112 probably due to the change in redox state of osmium tetroxide (Figure 1 – Figure  
113 Supplement 1c-f; see Methods). A similar effect was observed in erythrocytes, in which  
114 endogenous heme catalyzes the DAB reaction (Figure 1 – Figure Supplement 1g-j).

115

116 When the reduction protocol was applied to retinas, we were able to visualize RGCs  
117 that had been tagged with APX, APEX2-NES (APEX2 fused to a nuclear export signal)  
118 or erHRP (Fig. 1i-o, Figure 1 – Figure Supplement 2 and 3). As expected, APX and  
119 APEX2-NES labeled the cytoplasm diffusely (Fig. 1j) while erHRP labeled membrane-  
120 bound intracellular compartments (Fig. 1n). Thus they could be used as orthogonal  
121 labels, although we have not yet pursued this application. The strength of the signal  
122 allowed us to identify small stained dendritic profiles (Fig. 1k, o) and to view the  
123 terminals of RGCs in the superior colliculus, approximately 1 cm from the somata (Fig  
124 1l). Remarkably, the reduction protocol actually improved ultrastructural preservation  
125 irrespective of peroxidase expression or DAB treatment (Fig. 1h). Part of the  
126 improvement resulted from an increase in the reactivity of membranes to osmium,  
127 thereby enhancing membrane-cytoplasm contrast (Figure 1 – Figure Supplement 4).  
128 This improvement is also visible in the staining strength of synaptic densities (Figure 1 –  
129 Figure Supplement 4 a, b). When we asked blind-to-condition observers to judge the  
130 quality of synapses between both conditions, the reduced tissue was selected ~3 times  
131 more frequently than unreduced tissue (Figure 1 – Figure Supplement 4e). Thus, rather  
132 than sacrificing ultrastructure for reactivity or vice versa, this protocol improved both.

133

134 For the approach to be useful, it is essential that peroxidase expression does not affect  
135 synapse formation and that synaptic partners of peroxidase expressing cells can be  
136 identified. When analyzing our datasets, we could not detect any structural change in  
137 tissues expressing either of the peroxidases. The number of synapses counted in  
138 peroxidase expressing and control sections was also similar, 0.32 and 0.34 synapses /  
139  $\mu\text{m}^2$ , respectively. To test whether the electron dense precipitate hinders reliable  
140 synaptic identification, we characterized the synaptic connections received and made by  
141 APEX2 or erHRP expressing retinal ganglion cells (Figure 1k, o; Figure 1  
142 Supplementary Figure 5). Cells presynaptic to APEX2 or erHRP could be clearly  
143 identified based on ultrastructural details (Figure 1 Supplementary Figure 5a , c).  
144 Postsynaptic partners of APEX2-expressing cells could also be identified. Moreover,  
145 synaptic vesicles could often be identified in presynaptic terminals of APEX2-expressing  
146 neurons because they were unstained, and thereby contrasted with the electron-dense  
147 cytosol. However, the endoplasmic reticulum did not regularly extend to axonal  
148 terminals, making it difficult to identify postsynaptic partners of erHRP expressing  
149 ganglion cells.

150  
151 To test the generality of the method we expressed APEX fused to GFP in direction-  
152 selective tangential cells of *Drosophila melanogaster*<sup>17</sup> (*DB331-Gal4* → *UAS-APEX-*  
153 *GFP*; see Methods). This driver line expresses mainly in 6 vertically sensitive and 3  
154 horizontally sensitive tangential cells. This expression pattern was apparent using either  
155 GFP fluorescence or the polymerized DAB to mark the cells (Figure 2a, b). We were  
156 also able to visualize the electron dense precipitate of these processes in the fly's optic

157 lobes (Fig. 2c, d). Although our method was optimized for mammalian tissue,  
158 ultrastructural detail was reasonable (Figure 2e) and allowed the identification of  
159 synaptic contacts made by and onto APEX expressing cells (Figure 2f-h).

160

161 To implement sparse reconstruction, we used the ATUM<sup>18</sup> (automated tape-collecting  
162 ultra-microtome) to serially section retinas containing either APEX2-NES-expressing  
163 retinal ganglion cells (J-RGCs<sup>15</sup>) or retinal interneurons (starburst amacrine cells (SACs)  
164 labeled using Choline Acetyltransferase-Cre<sup>19</sup>. Because we could identify small  
165 peroxidase-stained neurites at overview resolution (20-30 nm per pixel), we tested the  
166 minimal requirements to reconstruct both cell types at these resolutions. Rapidly  
167 imaging every 10<sup>th</sup> section (270 nm separation), at 30 nm resolution was sufficient for  
168 mapping a J-RGC dendrite (144 sections covering >1x10<sup>7</sup> μm<sup>3</sup>, imaged in 22 hours; Fig.  
169 3a, b). By comparison, imaging the same volume at high resolution (4nm/pixel) would  
170 have taken ~2500 hours on the same microscope. Manual reconstruction of the J-RGC  
171 was straightforward and took 2 worker-hours (Fig. 3c). To extend this result to another  
172 cell type, we imaged all 1260 sections from a bloc with APEX2-NES-positive SACs and  
173 reconstructed SAC processes in this volume (Fig. 3d-f). Thus, we can reliably find and  
174 reconstruct genetically identified cells.

175

176 Although 20 nm resolution is sufficient for viewing neurites, it does not allow optimal  
177 visualization of synaptic contacts (Fig. 3g-h). However, sections generated using ATUM  
178 are collected on wafers, and can be re-imaged; a program, Wafer-Mapper<sup>18</sup>, facilitates  
179 returning to the same place on a given section with micron-level precision. This feature

180 allows targeted imaging at high resolution of areas chosen from the rapidly acquired,  
181 lower resolution reconstruction, thereby substantially reducing imaging time. To test this  
182 multi-scale approach, we focused on the SACs, whose dendrites can be less than 100  
183 nm in diameter. We selected a heavily-labeled  $\sim 5 \times 10^5 \mu\text{m}^3$  volume from the overview-  
184 resolution reconstruction of  $\sim 2 \times 10^7 \mu\text{m}^3$  and acquired a high-resolution (4 nm/pixel) data  
185 set in 250 hours (Fig. 3i). Compared to a completely high-resolution approach, this  
186 amounts to a 40-fold reduction in imaging time. More importantly, it expedited  
187 reconstruction, the current time-limiting step in connectomics<sup>8</sup>, by constraining efforts  
188 to defined regions of interest. We manually traced and reconstructed the SAC plexus in  
189 this volume, observing multiple SAC-SAC interactions, dendritic fasciculation in the SAC  
190 plexus and dendritic branching (Fig. 3j, k and data not shown).

191

192 Finally, to further expedite the reconstruction pipeline, we developed an algorithm that  
193 detects and segments APEX2-positive processes, taking advantage of the high contrast  
194 rendered by the DAB polymer. Our algorithm is fast, parameterized and does not rely on  
195 the supervised machine learning training regimes currently required for lower contrast  
196 material<sup>7</sup> (Figure 4a, Methods). We tested the algorithm using 401 sections from the  
197 high-resolution dataset (Fig. 3i). We hand-segmented a set of 444 APEX2 positive  
198 segments, and then compared these results to those obtained computationally. We  
199 calculated a recall statistic of 91.8% for the 2D segmentation portion of the algorithm  
200 (Fig. 4b,c). All missed segments were small (on average  $45 \times 42$  pixels), and were  
201 seldom necessary to establish connectivity. Consistent with human inferred  
202 segmentation, the analysis of segment adjacency in local neighborhoods can make

203 connections in regions with small gaps. To test the accuracy of the algorithm for longer  
204 ( $> 50 \mu\text{m}$ ) processes, we segmented and reconstructed a dendritic branch of a starburst  
205 amacrine cell. Our algorithm could reconstruct the main characteristics of the dendritic  
206 processes and recapitulated most of the manually segmented details (Figure 4d, e). The  
207 primary advantage of this approach is processing time, being two orders of magnitude  
208 faster than approaches based on convolutional neural networks for membrane  
209 classification<sup>7,20</sup>. Training regimes in the neural network approaches require adjusting  
210 at least thousands of parameters separately for each new tissue; in contrast, our  
211 algorithm incorporates unsupervised components with a small fixed set of tunable  
212 parameters (see Methods and Supplementary Code). Importantly, the high contrast-to-  
213 noise ratio of the peroxidase-labeled cells is the enabling factor for the efficacy of this  
214 algorithm, which means that it could be used for reconstruction of DAB-stained  
215 structures in any tissue. Thus, although detailed synaptic properties may be obscured  
216 by the electron-dense stain, our methods are well-suited for rapid reconstruction of  
217 targeted neuron morphology and connectivity.

218

219 In summary, we have assembled a set of tools that enables rapid reconstruction of  
220 genetically identified neurons, so that their shapes and connections can be mapped at  
221 high resolution in much less time than required for conventional imaging and  
222 segmentation protocols. By expediting the analysis of neural motifs, ARTEMIS renders  
223 the interrogation of diverse samples feasible and holds a clear promise to unravel  
224 mechanisms ranging from neuronal development to computations.

225

226 **MATERIALS AND METHODS**

227 **Animals.** Animals were used in accordance with NIH guidelines and protocols approved  
228 by Institutional Animal Use and Care Committee at Harvard University. *JAM-B-CreER*  
229 mice<sup>14</sup> were generated in our laboratory. *ChAT-cre* mice<sup>19</sup>, and *Cart-cre* mice<sup>21</sup> were  
230 obtained from Jackson Laboratories. In the *Chat-cre* line, Cre recombinase gene was  
231 targeted to the endogenous *Chat* gene; this line expresses Cre in starburst amacrine  
232 cells (SACs). In the *Cart-cre* transgenic line, Cre expression is controlled by regulatory  
233 elements from the *Cartpt* gene. In this line, Cre marks ON-OFF direction selective  
234 retinal ganglion cells. Mice were maintained on a C57/B6J background. Both male and  
235 female mice were used in this study. Animals were 60 to 100 days old at the time of  
236 euthanasia.

237

238 Flies were raised on standard cornmeal-agar medium. The DB331 Gal4-line<sup>17</sup> was  
239 kindly provided by Vivek Jayaraman (Janelia Research Campus) and the *UAS-APEX-*  
240 *GFP*<sup>22</sup> line was generated and kindly provided by Chiao-Lin Chen and Norbert  
241 Perrimon (Harvard Medical School and HHMI).

242

243 **Peroxidases.** The endoplasmic reticulum-targeted HRP (erHRP) was designed as  
244 follows. First, to improve expression in mammals, the nucleotide sequence of HRP  
245 (horseradish peroxidase from a plant, *Armoracia rusticana*) was codon-optimized  
246 (DNA2.0, Menlo Park, CA). Second, to regulate protein trafficking a signal secretion  
247 sequence from the human immunoglobulin kappa chain (from pDisplay, Invitrogen,  
248 Carlsbad, CA) as well as an endoplasmic reticulum (ER)-retention signal (-KDEL) were

249 appended at the N- and C-termini, respectively. Finally, the N175S mutation  
250 was introduced to confer heat stability and resistance to H<sub>2</sub>O<sub>2</sub><sup>23</sup>. The sequence of this  
251 cDNA is available from GenBank #KU504630. Ascorbate peroxidase (APX, dimeric)  
252 from pea<sup>12</sup>, and the enhanced monomeric version APEX2 (derived from soybean  
253 APEX)<sup>13</sup> were codon-optimized for better expression in mammals. In APEX2NES, the  
254 nuclear export signal (NES) was appended to APEX2. The erHRP, APX,  
255 and APEX2NES plasmids under CMV promoter were transfected to HEK293T cells  
256 (ATCC) using the DMRIE-C transfection reagent (Life Technologies). Subsequently,  
257 the cDNAs were cloned into a plasmid encoding a Cre-dependent Adeno-associated  
258 virus (AAV) backbone with the CAG (CMV-beta actin promoter + beta-globin leader)  
259 promoter, woodchuck post-transcriptional element (WPRE), and the FLEX switch<sup>24</sup>  
260 (Supplementary Table 1). AAV viruses were generated by transfecting these plasmids  
261 together with appropriate helper plasmids, and prepared using a chemical precipitation  
262 method<sup>25</sup>.

263

264 Plasmids encoding the viral vectors will be sent to Addgene ([www.addgene.org](http://www.addgene.org)) on  
265 acceptance of this paper.

266

267 **AAV-mediated gene transfer.** For viral-mediated gene transfer, adult Cre-mice were  
268 anaesthetized with ketamine/xylazine by intraperitoneal injection. A 30 1/2G needle  
269 was used to make a small hole in the temporal eye, below the cornea. 1µl of vitreous  
270 fluid was withdrawn and then 1µl of rAAV2 or rAAV2/9 Cre-dependent viruses (a titre of  
271 ~1 × 10<sup>11-12</sup> genome copies per ml) was injected into the subretinal space with a

272 Hamilton syringe and 33G blunt-ended needle. Animals were euthanized and retinas  
273 were dissected 4-6 weeks following injection.

274

275 **Tissue preparation.** Mouse retinas were dissected from eyecups in oxygenated Ames'  
276 medium (Sigma) with constant bubbling (95% O<sub>2</sub>, 5% CO<sub>2</sub>) at room temperature. Four  
277 incisions were made to flat-mount the retina with ganglion cells facing up onto  
278 nitrocellulose filter paper. The tissue was drop-fixed, with 2% PFA and 2.5 %  
279 glutaraldehyde followed by 2.5 % glutaraldehyde (times specified in Supplementary  
280 Table 2) then washed. HEK-cells were fixed with 2% PFA and 2.5 % glutaraldehyde for  
281 15 min followed by a 45 min fix in 2.5 % glutaraldehyde. Flies were decapitated and  
282 dissected in oxygenated Ringer solution. A small incision was made on the back of the  
283 head and the posterior cuticle was separated from the head. This ensured that the  
284 fixative and staining solutions could penetrate into the brain while the rest of the cuticle  
285 protected brain tissue during processing. Flies were fixed with 2% PFA and 2.5 %  
286 glutaraldehyde for 15 min followed by a 45 min fix in 2.5 % glutaraldehyde. Following  
287 aldehyde fixation, cells and tissues were washed, reacted with DAB to reveal sites of  
288 peroxidase activity, washed again, reduced with 50 mM sodium hydrosulfite and stained  
289 with osmium. Osmium treatments included 2% aqueous osmium tetroxide (used only in  
290 HEK cell micrographs of Fig.1 Supplementary Fig. 1) or the reduced osmium tetroxide-  
291 thiocarbohydrazide (TCH)-osmium (“rOTO”)<sup>26-28</sup> protocol (all other Figures). Due to the  
292 two consecutive osmication steps, the “rOTO” protocol improves the signal of  
293 membranes compared to the aqueous osmium. This enables reasonable signal-to-noise  
294 ratios at high scanning, an essential requirement our approach. Finally, the stained

295 tissue was dehydrated and infiltrated with Durcupan resin. Sodium-cacodylate (cat. no.  
296 12300), glutaraldehyde (16220 and 16120), paraformaldehyde (15710), osmium  
297 tetroxide (19190), maleic acid (18150), acetone (glass distilled; 10015) and uranyl  
298 acetate (22400) were purchased at Electron Microscopy Sciences (EMS); AMES  
299 medium (A1420), 3,3'-diaminobenzidine (DAB; D5905), potassium hexacyanoferrate (II)  
300 (P9387), thiocarbohydrazide (88535), sodium hydrosulfite (157953) and durcopan resin  
301 (44610) were purchased at Sigma-Aldrich. Concentrations and incubations times, along  
302 with details on reagents are provided in Supplementary Tables 2 and 3.

303

304 **Immunohistochemistry.** For the image in Figure 2a, the fly brain was fixed in 2%  
305 paraformaldehyde in PBS for 30 min on ice, washed with PBS and blocked with 3%  
306 goat serum/1% Triton X-100/PBS. For staining, tissue was incubated with 3% goat  
307 serum/1% Triton X-100/PBS and rabbit anti-GFP Alexa Fluor 488 conjugate (dilution  
308 1:1000, Invitrogen, A-21311) at 4°C for 1 days and washed with PBS. Brains were  
309 mounted on Vectashield mounting medium (Vectorlabs) and imaged in a confocal  
310 microscope (Olympus FVA). For the image in Figure 2b, brains were prepared for  
311 electron microscopic and imaged before osmication.

312

313 **Electron microscopy.** The cured blocks were trimmed to a 2 x 3 mm rectangle and a  
314 depth of 400 µm and then readied for automated serial sectioning. The automated,  
315 unattended collection of ~ 30 nm serial sections was accomplished using a custom tape  
316 collection device (ATUM)<sup>18</sup> attached to a commercial ultramicrotome. The sections were  
317 collected on plasma-treated carbon-coated polyamide (Kapton, Sheldahl) 8-mm-wide

318 tape. Sections were post-stained with 1% uranyl acetate in maleate buffer for 30 s and  
319 with 3% Lead Citrate (Ultrostain II; Leica - cat. no. 16707235) for 30 s. An automated  
320 protocol to locate and image sections on the wafers was used<sup>18</sup> with a Sigma scanning  
321 electron microscope (Carl Zeiss), equipped with the ATLAS software (Fibics). Images  
322 were acquired using secondary electron detection.

323

324 For the medium- and high-resolution data sets, non-affine alignment was accomplished  
325 through the FijiBento alignment package (<https://github.com/Rhoana/FijiBento>) that  
326 enables the alignment of large data sets in a relatively short period of time. To this end,  
327 the alignment was performed on the Odyssey cluster supported by the FAS Division of  
328 Science, Research Computing Group at Harvard University. The aligned images were  
329 then manually segmented using a custom volume annotation and segmentation tool  
330 (VAST; <http://openconnecto.me/Kasthuri2014/Code/VAST>). The segmented images  
331 were processed for data analysis and 3D modeling with Matlab scripts, and Persistence  
332 of Vision™ Raytracer (<http://www.povray.org/>) for rendering steps.

333

334 **Automatic 2D Segmentation and 3D Reconstruction.** Full resolution EM images  
335 (100000 x 50000 pixels) underwent contrast adjustment via histogram equalization to  
336 normalize image intensities across slices. For each normalized image, a global  
337 threshold  $\tau$  was computed via clustering-based image analysis <sup>29</sup>, modulated by the  
338 known contrast-enhanced pixel ranges of the ARTEMIS markers for a data set (e.g., for  
339 Suppl. Fig. 4b: if  $\tau < 0.6$ ,  $\tau = \tau * 0.82$ , else  $\tau = \tau * 0.86$ ). The normalized images were  
340 then converted to a binary representation, and clustering-based image thresholding was

341 applied again, assuming two classes (positive and negative), to gather 2D candidate  
342 segments. To remove artifacts such as speckle noise, and holes in the tissue, only  
343 segments that satisfy the following constraints were stored: 3 pixels < area < 130,000  
344 pixels and major axis length < 900 pixels. The remaining segments were assigned a  
345 unique label, and stored in a MySQL database, along with their coordinates and other  
346 geometric properties Based on the expected morphological progression of each process,  
347 irregularly large imaging artifacts that appear between adjacent segments in the volume  
348 were pruned. Graph-based segment search over the database entries established the  
349 connectivity between segments, including those with gaps in space between them, by  
350 finding the minimum distance between centroid points from all pairs of segments in a  
351 local neighborhood using a k-Nearest Neighbors-like<sup>30</sup> algorithm ( $k = 2$ ). Using the  
352 graph as a guide, 2D segments were merged into the final 3D reconstruction. We  
353 included the source code in the supplementary information, packaged up as a Matlab  
354 live script, with example images and an animation.

355

356 **Data.** All relevant data is available on request. The electron microscopic data set of Fig.  
357 3k, which includes the segmented processes used for the reconstructions, has been  
358 deposited to Dryad. DOI:10.5061/dryad.h67t6.

359

## 360 **ACKNOWLEDGMENTS**

361 We thank Alice Ting, Jeff Martell, and Stephanie Lam for advice and for providing the  
362 APX and APEX2 constructs. We also thank Chiao-Lin Chen and Norbert Perrimon for  
363 generating and providing the *UAS-APEX-GFP* fly and Benjamin de Bivort for support

364 with the fly work. This work was supported by NIH grant NS76467 to M.M., J.L. and  
365 J.R.S., an HHMI Collaborative Innovation Award to J.R.S., an IARPA contract  
366 #D16PC00002 to W.J.S. and by The International Human Frontier Science Program  
367 Organization fellowship to M.J. The authors declare no conflicts of interest.

368

369

370 **REFERENCES**

- 371
- 372 1. Wickersham, I. R. & Feinberg, E. H. New technologies for imaging synaptic  
373 partners. *Current opinion in neurobiology* **22**, 121–7 (2012).
- 374 2. Tønnesen, J. & Nägerl, U. V. Superresolution imaging for neuroscience.  
375 *Experimental neurology* **242**, 33–40 (2013).
- 376 3. Briggman, K. L., Helmstaedter, M. & Denk, W. Wiring specificity in the direction-  
377 selectivity circuit of the retina. *Nature* **471**, 183–8 (2011).
- 378 4. Bock, D. D. *et al.* Network anatomy and in vivo physiology of visual cortical neurons.  
379 *Nature* **471**, 177–82 (2011).
- 380 5. Takemura, S. Y. *et al.* A visual motion detection circuit suggested by *Drosophila*  
381 connectomics. *Nature* **500**, 175–81 (2013).
- 382 6. Morgan, J.L., Berger, D.R., Wetzel, A.W., & Lichtman, J.W. The fuzzy logic of  
383 neuronal connectivity in the mouse visual thalamus. *Cell* (in press).
- 384 7. Kasthuri, N. *et al.* Saturated Reconstruction of a Volume of Neocortex. *Cell* **162**,  
385 648–61 (2015).
- 386 8. Plaza, S. M., Scheffer, L. K. & Chklovskii, D. B. Toward large-scale connectome  
387 reconstructions. *Current opinion in neurobiology* **25**, 201–10 (2014).
- 388 9. Li, J., Wang, Y., Chiu, S.-L. L. & Cline, H. T. Membrane targeted horseradish  
389 peroxidase as a marker for correlative fluorescence and electron microscopy  
390 studies. *Front Neural Circuits* **4**, 6 (2010).
- 391 10. Atasoy, D. *et al.* A genetically specified connectomics approach applied to long-  
392 range feeding regulatory circuits. *Nat. Neurosci.* **17**, 1830–9 (2014).

- 393 11. Schikorski, T., Young, S. M. & Hu, Y. Horseradish peroxidase cDNA as a marker for  
394 electron microscopy in neurons. *J. Neurosci. Methods* **165**, 210–5 (2007).
- 395 12. Martell, J. D. *et al.* Engineered ascorbate peroxidase as a genetically encoded  
396 reporter for electron microscopy. *Nat. Biotechnol.* **30**, 1143–8 (2012).
- 397 13. Lam, S. S. *et al.* Directed evolution of APEX2 for electron microscopy and proximity  
398 labeling. *Nat. Methods* **12**, 51–4 (2015).
- 399 14. Kay, J. N. *et al.* Retinal ganglion cells with distinct directional preferences differ in  
400 molecular identity, structure, and central projections. *J. Neurosci.* **31**, 7753–62  
401 (2011).
- 402 15. Kim, I.-J. J., Zhang, Y., Yamagata, M., Meister, M. & Sanes, J. R. Molecular  
403 identification of a retinal cell type that responds to upward motion. *Nature* **452**, 478–  
404 82 (2008).
- 405 16. Bahr, G. F. Osmium tetroxide and ruthenium tetroxide and their reactions with  
406 biologically important substances. Electron stains. III. *Exp. Cell Res.* **7**, 457–79  
407 (1954).
- 408 17. Joesch, M., Plett, J., Borst, A. & Reiff, D. F. Response properties of motion-  
409 sensitive visual interneurons in the lobula plate of *Drosophila melanogaster*. *Curr.*  
410 *Biol.* **18**, 368–74 (2008).
- 411 18. Hayworth, K. J. *et al.* Imaging ATUM ultrathin section libraries with WaferMapper: a  
412 multi-scale approach to EM reconstruction of neural circuits. *Front Neural Circuits* **8**,  
413 68 (2014).
- 414 19. Rossi, J. *et al.* Melanocortin-4 receptors expressed by cholinergic neurons regulate  
415 energy balance and glucose homeostasis. *Cell Metab.* **13**, 195–204 (2011).

- 416 20. Kaynig, V. *et al.* Large-scale automatic reconstruction of neuronal processes from  
417 electron microscopy images. *Medical image analysis* **22**, 77–88 (2015).
- 418 21. Madisen, L. *et al.* A robust and high-throughput Cre reporting and characterization  
419 system for the whole mouse brain. *Nat. Neurosci.* **13**, 133–40 (2010).
- 420 22. Morawski, B., Quan, S. & Arnold, F. H. Functional expression and stabilization of  
421 horseradish peroxidase by directed evolution in *Saccharomyces cerevisiae*.  
422 *Biotechnol. Bioeng.* **76**, 99–107 (2001).
- 423 23. Chen, C.-L. L. *et al.* Proteomic mapping in live *Drosophila* tissues using an  
424 engineered ascorbate peroxidase. *Proceedings of the National Academy of  
425 Sciences of the United States of America* **112**, 12093–8 (2015).
- 426 24. Atasoy, D., Aponte, Y., Su, H. H. & Sternson, S. M. A FLEX switch targets  
427 Channelrhodopsin-2 to multiple cell types for imaging and long-range circuit  
428 mapping. *J. Neurosci.* **28**, 7025–30 (2008).
- 429 25. Guo, P. *et al.* Rapid and simplified purification of recombinant adeno-associated  
430 virus. *J. Virol. Methods* **183**, 139–46 (2012).
- 431 26. Willingham, M. C. & Rutherford, A. V. The use of osmium-thiocarbohydrazide-  
432 osmium (OTO) and ferrocyanide-reduced osmium methods to enhance membrane  
433 contrast and preservation in cultured cells. *The journal of histochemistry and  
434 cytochemistry : official journal of the Histochemistry Society* **32**, 455–60 (1984).
- 435 27. Hua, Y., Laserstein, P. & Helmstaedter, M. Large-volume en-bloc staining for  
436 electron microscopy-based connectomics. *Nat Commun* **6**, 7923 (2015).
- 437 28. Tapia, J. C. *et al.* High-contrast en bloc staining of neuronal tissue for field emission  
438 scanning electron microscopy. *Nat Protoc* **7**, 193–206 (2012).

439 29. Bankman, I. Handbook of medical image processing and analysis. Academic Press,  
440 Second Edition (2008).

441 30. Hastie, T, Tibshirani, R & Friedman, J. The Elements of Statistical Learning.  
442 Springer-Verlag, Second Edition (2009).

443

444

445

446 **FIGURE LEGENDS**

447

448 **Figure 1. Enhanced staining of genetic encoded tags for EM.**

449 **a-b.** Bright-field images of HEK-cells rendered photon-dense by DAB polymerization,  
450 catalyzed either by APEX2 tagged with a nuclear export signal (APEX2-NES) (**a**) or  
451 endoplasmic reticulum tagged HRP (erHRP) (**b**).

452 **c-d.** Bright-field images of direction-selective retinal ganglion cells (ooDSGC)  
453 expressing APEX2-NES (**c**) or erHRP (**d**) and rendered photon-dense as in (**a**).

454 **e.** Enhanced staining strategy.

455 **f-g.** EM-micrographs of HEK-cells rendered electron-dense after DAB-polymerization as  
456 in (**a**). A standard EM staining protocol showed no detectable cytosolic DAB-polymer  
457 staining (**f**), whereas the addition of a reduction step dramatically enhanced DAB-  
458 polymer staining (**g**).

459 **h.** Ribbon synapses in the outer plexiform layer; ultrastructure is well preserved after  
460 reduction.

461 **i.** EM-micrograph of an ooDSGC somata (arrowhead) rendered electron dense after  
462 tissue reduction next to a non-expressing RGC (asterisk).

463 **j.** Close-up of cytosolic APEX2 staining.

464 **k.** Dendritic processes expressing APEX2 (asterisk) contacted by presynaptic partner  
465 (arrowhead) in the inner plexiform layer.

466 I. Axonal long-range projections of APEX2-expressing ooDSGC in the superior  
467 colliculus (asterisk) with a postsynaptic target (arrowhead).

468 m. erHRP-expressing (arrowhead) RGC next to a non-expressing RGC (asterisk).

469 n,o. Close-up of erHRP staining of a J-RGC soma (n) and dendrite (o) (arrowhead point  
470 to presynaptic partners).

471 c,d,i-l are from *Cart-Cre* mice; m-o from *Jam-B-CreER* mice.

472 Scale bars: a-d: 25  $\mu$ m; f-g: 10  $\mu$ m; l, m: 5  $\mu$ m; h, j-l, n,o: 500 nm;

473

474 **Figure 2. APEX expressing interneurons in *Drosophila melanogaster*.**

475 a. Fluorescent image of a brain of *Drosophila melanogaster* (*DB331-Gal4*  $\rightarrow$  UAS-  
476 APEX-GFP) expressing APEX in direction-selective lobula plate tangential cells  
477 (LPTCs).

478 b. Bright field image of a similar plane from another (*DB331-Gal4*  $\rightarrow$  UAS-APEX-GFP)  
479 fly, labeled with DAB.

480 c. Electron micrograph of a frontal brain section (30 nm thickness) containing Electron  
481 dense staining in axonal processes of LPTCs (arrowhead and framed box).

482 d. Enlarged view of the framed region in (c). Arrows point to electron dense processes.

483 e. Unstained synaptic terminal, showing quality of ultrastructural detail.

484 f. Synaptic nerve terminal in an APEX-positive process, identifiable by contrast-reversed  
485 vesicles.

486 g,h. APEX-positive postsynaptic processes, identifiable by the presence of adjacent  
487 vesicle-laden, T-bar-containing terminals.

488 Scale bars: **a-c**: 100  $\mu\text{m}$ ; **d**: 10  $\mu\text{m}$ ; **e-g**: 500 nm.

489

490 **Figure 3. Targeted interrogation of serial-section EM volumes in mouse retina.**

491 **a.** Overview-resolution EM volume containing J-RGCs expressing APEX2-NES. Every  
492 10<sup>th</sup> section was imaged at 30 nm/pixel.

493 **b.** Two consecutive sections containing APEX2-NES expressing J-RGC processes  
494 (arrows).

495 **c.** Reconstructed J-RGC. Note the reduced complexity of the dendritic field due to the  
496 subsampling of the overview dataset.

497 **d.** Overview-resolution EM volume that contains SACs expressing APEX2-NES.  
498 Sections were imaged at 20 nm/pixel.

499 **e.** Two consecutive sections showing a SAC-SAC contact (arrowheads).

500 **f.** Reconstruction of the SAC-SAC interaction in (**e**); arrowhead indicates contact shown  
501 in **e**.

502 **g-h.** Comparison of ultrastructural detail visible at 20nm/pix (**g**) or 4 nm/pix (**h**). Although  
503 both images contain ribbon synapses, the low-resolution image (**g**) lacks the required  
504 resolution to identify it. Arrowheads point to ribbons.

505 **i.** High-resolution (4 nm/pixel) EM subvolume selected from (**d**).

506 **j.** Two high-resolution EM-micrographs containing SAC-processes expressing APEX2-  
507 NES receiving synaptic contacts (arrowheads).

508 **k.** Reconstruction of the SAC plexus with its characteristic dendritic fasciculation and  
509 net-like structure. Asterisk indicates contact and arrowheads the synaptic inputs shown  
510 in **j** (top panel).

511 Scale bars: **b**: 5 µm; **c**: 50 µm; **e, j**: 1 µm; **g-h**: 200 nm.

512

513 **Figure 4. Automatic segmentation and reconstruction algorithm for APEX2**

514 **positive processes.**

515 **a.** The algorithm performs unsupervised 2D segmentation and 3D reconstruction

516 without the need of pre-training. The procedure follows these steps (shown above): **1.**

517 Clustering-based image thresholding over pixel intensities from known contrast-

518 enhanced ranges, modulated via quality assessment; **2.** 2D segmentation based on

519 unsupervised clustering; **3.** Calculation of geometric properties for each identified

520 segment, followed by noise and artifact pruning based on these properties; **4.**

521 Identification of large segments based on segment properties; **5.** Graph-based segment

522 search for reconstruction and labeling in 3D, followed by a final merging procedure to

523 enforce consistency across the volume. The improved contrast-to- noise ratio induced

524 by ARTEMIS is the enabling factor for the efficacy of this algorithm, which means

525 reconstructions can generalize beyond neuronal processes to any DAB stained tissue.

526 **b.** Unsupervised automatic segmentation of mouse SAC processes. Top: manual

527 segmentation, ground-truth; bottom: automatic segmentation.

528 **c.** Reconstructions of the dendritic process in **(b)**, comparing manual (top) and

529 automatic reconstructions.

530 **d.** Manual reconstruction of a starburst amacrine cell process. *En face* (top) and side

531 view (bottom).

532 **e.** Automatic reconstruction of the same process shown in **d**. *En face* (top) and side

533 view (bottom).

534 Scale bar in **b**: 1  $\mu\text{m}$ ; d, e: 10  $\mu\text{m}$ .

535

536 **SUPPLEMENTARY FIGURE LEGENDS**

537

538 **Figure 1 – Figure Supplement 1. DAB-polymer enhancement.** **a.** EM-micrograph of  
539 an APEX2-NES expressing process. Long DAB reaction times (5 hours) allowed  
540 visualizing the DAB-polymer using a standard EM-staining protocol, but severely  
541 deteriorated the quality of the ultrastructure.

542 **b.** EM-micrograph of a RGC using a fixation and staining protocol optimized to preserve  
543 good ultrastructure. Under these conditions, DAB-polymer signals were absent or very  
544 week, as exemplified by the weakly stained somata (encircled with asterisk) and its  
545 corresponding unstained process (encircled).

546 **c-f.** EM-micrograph of APEX2-NES expressing HEK-cells fixed with the same protocol  
547 used for retinas and stained for EM after the DAB reaction. Four conditions were tested:  
548 the osmium only (**c,d**) or rOTO stainings (**e,f**) with the standard and reduction protocol  
549 (see Methods). Using the standard protocol, no or very week signal was detected using  
550 the osmium (**c**) or the rOTO (**e**) staining, respectively. Asterisks in (**e**) depict weakly  
551 stained HEK-cell. In contrast, reducing the tissue dramatically enhanced the signal in  
552 both conditions (**d & f**).

553 **g-h.** Bright-field images of erythrocytes in retinal tissue after DAB-polymerization  
554 (arrowheads) before (**g**) and after the reduction step (**h**). The heme content in  
555 erythrocytes catalyzes the DAB reaction producing a strong precipitate that is enhanced  
556 by a reduction step.

557 **i-j.** EM-micrograph of erythrocytes using the rOTO staining protocol in standard (**i**) and  
558 reduced (**j**) conditions. The reduction enhances the DAB-polymer's affinity to osmium.

559 Scale bars: **a**: 1  $\mu\text{m}$ ; **b**: 5  $\mu\text{m}$ ; **c-f**: 10  $\mu\text{m}$ ; **g-h**: 20  $\mu\text{m}$ ; **i-j**: 5  $\mu\text{m}$ .

560

561 **Figure 1 – Figure Supplement 2. Cytosolic APEX2**

562 EM-micrograph of a mouse direction selective RGC soma rendered electron dense after  
563 tissue reduction (arrowhead). Note the small process visible in the inner plexiform layer  
564 (boxes, enlarge image on the right) and the strong signal of the erythrocytes (asterisk).

565 Scale bar: 10  $\mu\text{m}$ .

566

567 **Figure 1 – Figure Supplement 3. Endoplasmic reticulum tagged HRP (erHRP).**

568 **a.** Bright-field images of Cre-dependent virally infected mouse direction-selective retinal  
569 ganglion cell (ooDSGC) expressing erHRP and rendered photon-dense.

570 **b.** EM-micrograph of a vertical retinal cross-section with an erHRP expressing RGC.  
571 Asterisk depicts erHRP-expressing somata. GCL: ganglion cell layer, IPL: inner  
572 plexiform layer, INL, inner nuclear layer, OPL, outer plexiform layer, ONL, outer nuclear  
573 layer, PL: photoreceptor layer.

574 **c.** erHRP expressing somata.

575 **d-e.** erHRP expressing dendritic compartments in the IPL.

576 **f.** Micrograph of ribbon synapses in the IPL (arrowheads). Ultra-structural quality is  
577 preserved.

578 Scale bars: **a**: 20  $\mu\text{m}$ ; **b**: 10  $\mu\text{m}$ ; **c**: 5  $\mu\text{m}$ ; **d**: 1  $\mu\text{m}$ ; **e-f**: 500 nm.

579 **Figure 1 – Figure Supplement 4. Chemical tissue reduction improves contrast-to-**  
580 **noise ratio between membrane and cytosol.**

581 **a-b.** EM-micrographs of the inner plexiform layer of mouse retinas not treated with DAB  
582 and stained with the standard (**a**) or reduction protocol (**b**). Note the enhancement of the  
583 membrane and synaptic density stain in (**b**) compared to (**a**).

584 **c-d.** Intensity histograms of manually selected membrane or cytosol pixels from  
585 standard and reduced EM micrographs. The reduction shifts the distribution of the  
586 membrane pixels (black traces) by 24 intensity values to a lower mean value (□□  
587 compared to the cytosolic distribution (grey traces; Intensity values: 0 = dark; 255 =  
588 white). Thus, the reduction step increases the electron density of membranes  
589 specifically. Orange traces: Gaussian fits. The contrast-to-noise value is defined as:

$$CNR = \frac{\mu_2 - \mu_1}{\sqrt{\sigma_2^2 + \sigma_1^2}}$$

590 Contrast-to-noise improves by 62 % by reducing the tissue and therefore could be  
591 valuable signal enhancing step to improve automatic segmentation results that are  
592 based on machine-learning approaches.

593 **e.** Blind-to-condition selection of synaptic quality based on randomized pairwise  
594 comparisons.

595 Scale bar: 1  $\mu$ m.

596

597

598 **Figure 1 – Figure Supplement 5. Synaptic contacts received and made by**  
599 **peroxidase expressing cells.**

600 **a.** EM-micrographs of the inner plexiform layer of mouse retinas expressing APEX2 in  
601 ooDS ganglion cells contacted by presynaptic partners (arrowheads).

602 **b.** EM-micrographs of the upper layers of the superior colliculus with including axonal  
603 termini of APEX2 in ooDS ganglion cells contacting by postsynaptic partners  
604 (arrowheads).

605 **c.** EM-micrographs of the inner plexiform layer of retinas expressing erHRP in ganglion  
606 cells (asterisks) contacted by presynaptic partners (arrowheads).

607 Scale bars: 500 nm

608

609 **Supplementary File 1. AAV constructs used in this study.**

610

611 **Supplementary File 2. Fixation, reaction and staining method: rOTO protocol**

612

613 **Supplementary File 3. Fixation, reaction and staining method: reduced osmium**  
614 **protocol**

615

616 **Supplementary File. 4 Table of Contents - Artemis Live Scripts.mlx**

**Figure 1**

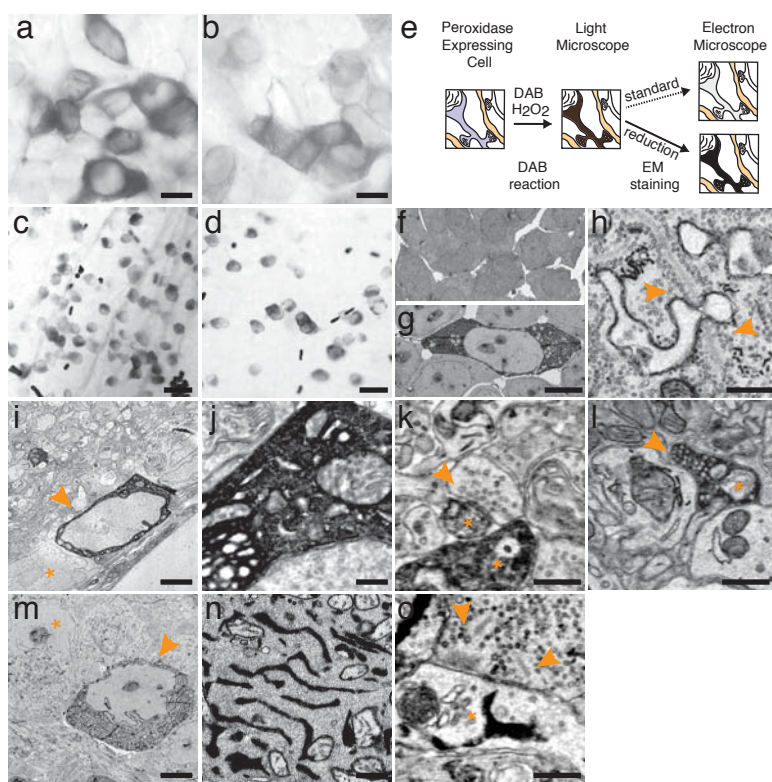
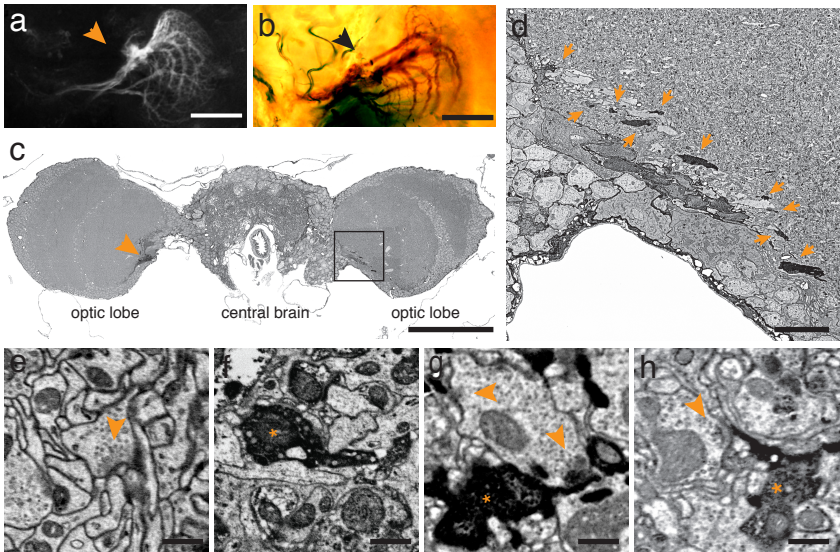
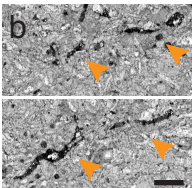
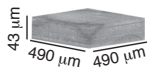


Figure 2

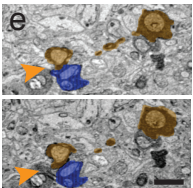
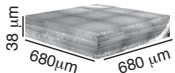


# Figure 3

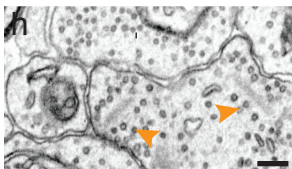
a



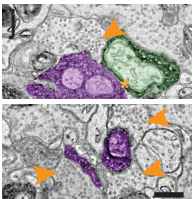
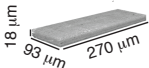
d



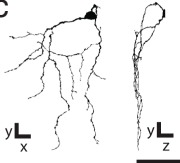
g



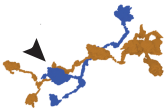
i



c



f



k

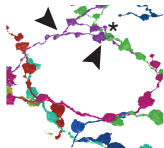


Figure 4

